1. Title page

Multimodal loading environment predicts bioresorbable vascular scaffolds' durability

*Pei-Jiang Wang[1], *Francesca Berti[1,2], Luca Antonini[2], Farhad Rikhtegar Nezami[1], Lorenza Petrini[3], Francesco Migliavacca[1,2], and Elazer R. Edelman[1,4]

[1] Institute for Medical Engineering & Science, Massachusetts Institute of Technology, Cambridge, Massachusetts, 02139, USA.
[2] Laboratory of Biological Structure Mechanics, Department of Chemistry, Materials and Chemical Engineering 'Giulio Natta', Politecnico di Milano, Milan, Italy
[3] Department of Civil and Environmental Engineering, Politecnico di Milano, Milan, Italy.
[4] Cardiovascular Division, Department of Medicine, Brigham and Women's Hospital, Harvard Medical School, Boston, Massachusetts, 02115, USA.
* These authors contribute equally.

Author email address:
Pei-Jiang Wang: wpj@bu.edu
Francesca Berti: francesca.berti@polimi.it
Luca Antonini: luca.antonini@polimi.it
Farhad Rikhtegar Nezami: farhadr@mit.edu
Lorenza Petrini: lorenza.petrini@polimi.it
Francesco Migliavacca: francesco.migliavacca@polimi.it
Elazer R. Edelman: ere@mit.edu

Corresponding Author:
Pei-Jiang Wang
77 Massachusetts Avenue, Building E25-442, Cambridge, MA 02139. USA.
Tel: +1 734-358-5085
E-mail: wpj@bu.edu

2. Abstract and key terms

Bioresorbable vascular scaffolds were considered the fourth generation of endovascular implants deemed to revolutionize cardiovascular interventions. Yet, unexpected high risk of scaffold thrombosis and post-procedural myocardial infractions quenched the early enthusiasm and highlighted the gap between benchtop predictions and clinical observations. To better understand scaffold behavior in the mechanical environment of vessels, animal, and benchtop tests with multimodal loading environment were conducted using industrial standard scaffolds. Finite element analysis was also performed to study the relationship among structural failure, scaffold design, and load types. We identified that applying the combination of bending, axial compression, and torsion better reflects incidence observed *in vivo*, far more than tranditional single mode loads. Predication of fracture locations is also more accurate when at least bending and axial compression are applied during benchtop tests (>60% fractures at connected peak). These structural failures may be initiated by implantation-induced microstructural damages and worsened by cyclic loads from the beating heart. Ignoring the multi-modal loading environment in benchtop fatigue tests and computational platforms can lead to undetected potential design defects, calling for redefining consensus evaluation strategies for scaffold performance. With the robust evaluation strategy presented herein, which exploits the results of *in-vivo*, *in-vitro* and *in-silico* investigations, we may be able to compare alternative designs of prototypes at the early stages of device development and optimize the performance of endovascular implants according to patients-specific vessel dynamics and lesion configurations in the future.

53 Key terms: coronary stents/scaffolds, polylactic acid, polymer mechanics, finite
54 element, animal study, scaffold fracture, patient-specific, design optimization

3. Introduction

Endovascular support has evolved with innovations in materials science, device design, manufacturing technology, and composite pharmacology from balloons to bare-metal stents (BMS) and drug-eluting stents (DES) [2,12,15]. Each successive refinement has helped overcome clinical complications associated with early generation devices to make this technology the golden standard in treating obstructive atherosclerotic vascular diseases [5,6]. However, permanent indwelling devices may forever impede complete vascular repair, causing long-term complications such as vessel caging, alteration of vasomotor tone, the limited possibility of re-intervention, and vessel rupture from strut fracture [14]. These fundamental limitations drove the community toward bioresorbable scaffolds (BRS), which can provide temporary vascular scaffolding and then erode away, leaving an intact vessel and theoretically reducing long-term complications associated with permanent implants. Yet, mounting evidence from clinical trials showed that early generations of BRS were associated with a substantially higher incidence of thrombosis and greater incidences of myocardial infarctions [1,16]. This unexpected finding highlighted the gap between benchtop predictions and clinical observations, and the poorly understood BRS behaviors in a physiological environment.

A part of the inadequate clinical performance of this technology arises from limitations in materials and design. Recent studies that focused on BRS microstructure and mechanics have provided insight into potential failure mechanisms at different time scales [7,18,19]. Localized structural irregularities that arise from stress concentration were identified almost immediately upon crimping and inflation, leading to early loss of structural integrity [19]. Accelerated asymmetric material degradation from spatial

heterogeneity in material microstructures exacerbates these deformations and may cause severe hemodynamic disruption in the long-term [18].

Acute and sub-acute strut malapposition and overhanging were also observed [17], indicating a new, under-investigated failure mode. Such failure may arise due to the continuous exposure to cyclic loads from the motion of the heart, and probably even more profound in BRS as the degradation of this device also depends on external loading conditions. Consensus standard methods for evaluating scaffold durability apply single-mode cyclic loads such as radial pulsation, bending, or uniaxial tension to pristine simplified geometries or scaffolds [3,4,11]. However, scaffolds not only experience complex multimodal loads, such as axial compression, torsion, and bending [8–10,13], but also are subject to critical stresses from implantation [18,19]. Overlooking the complex, physiological loading environment and the load history can limit the design of safe devices and may lead to unexpected adverse clinical outcomes.

In this work, we employed a multimodal scaffold tester to conduct fatigue tests on two different scaffold designs under various combinations of loads. We successfully reproduced results from animal studies in terms of fracture rates and locations when physiologically relevant loads, including axial compression, bending, and torsion were applied. We then created a digital twin of the multimodal benchtop test to evaluate the role of the stress field induced by both the crimping/inflation of the scaffold and the applied cyclic loads. Finite element (FE) analyses evaluate the stress distribution in the scaffolds subjected to different combinations of loads. It was then possible to understand the relationship between structural failure, scaffold design, and load types.

4. Materials and Methods

Fully resorbable poly-l-lactic acid (pLLA) scaffold systems provided by Boston Scientific Corporation (BSC) were used in all experimental and computational studies. All tested units were prototypes under development and not commercially available. The system consists of a catheter, a guidewire, a noncompliant balloon, and a crimped polymeric scaffold. The scaffold is 16 mm in length, 3.0 mm in inner diameter after inflation at nominal pressure (10 atm), and with a wall thickness of 110 μm. Two designs, slot and non-slot (Figure 1), were investigated.

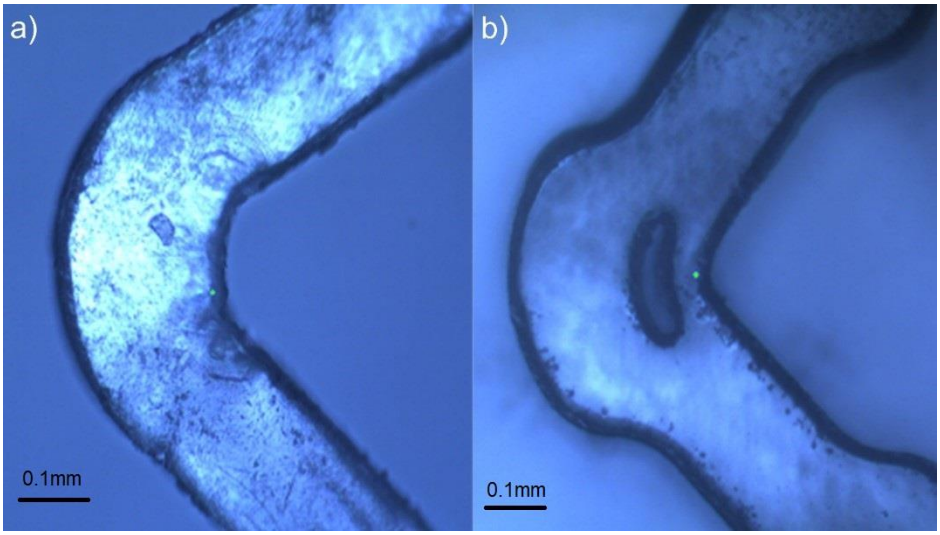

Figure 1 Representative region of (a) non-slot and (b) slot design scaffold.

4.1 Pre-clinical Studies on Scaffold Fractures

A porcine model served to provide insight into the fracture performance of BRS with different designs implanted in coronary arteries. Six Yorkshire porcine (castrated male or post-menopausal female, 40 – 50 kg) were sedated with an intramuscular injection of Telazol at 3.5 – 5.5 mg/kg, endotracheally intubated and maintained under general anesthesia with inhaled isoflurane. 325 mg of Aspirin and 150 mg of Clopidogrel were

given via oral administration prior to the procedure for antiplatelet purposes. Heparin was administering at 20 – 400 IU/kg every 30 – 45 min during the procedure to elevate the activated clotting time above 250 seconds. Animals were maintained in accordance with the American Preclinical Services Standard of Procedure (APS SOP) and monitored by continuous recording of oxygen saturation, heart rate, and blood pressure.

Up to three scaffolds, one in each coronary artery (left anterior descending, left circumflex, and right coronary artery), were implanted in each animal. The target vessel size was 2.50 – 3.50 mm in diameter. No significant difference existed in dimension between distinct vessels. Optimal implantation targeted a scaffold inner diameter to artery ratio of 1.1 – 1.15: 1.0, using the mean vessel segment diameter as determined by quantitative coronary arteriography (QCA). Optical coherence tomography (OCT) was used to determine proper scaffold apposition after initial scaffold deployment. If malposition was noted, post-dilation with balloon was performed. At the end of the study, sixteen (8 slot and 8 non-slot design) scaffolds were implanted

The overall length of the study was 30 days per implanted scaffold. Since the degradation mechanism of PLLA is primarily passive hydrolysis which takes months to years, minimum degradation would have started at this time point. Scaffold fracture analysis was performed via dissection microscope and Visicon imaging after scaffolded vessel excision from the heart.

4.2 Durability Test with Multimodal Loading Environment

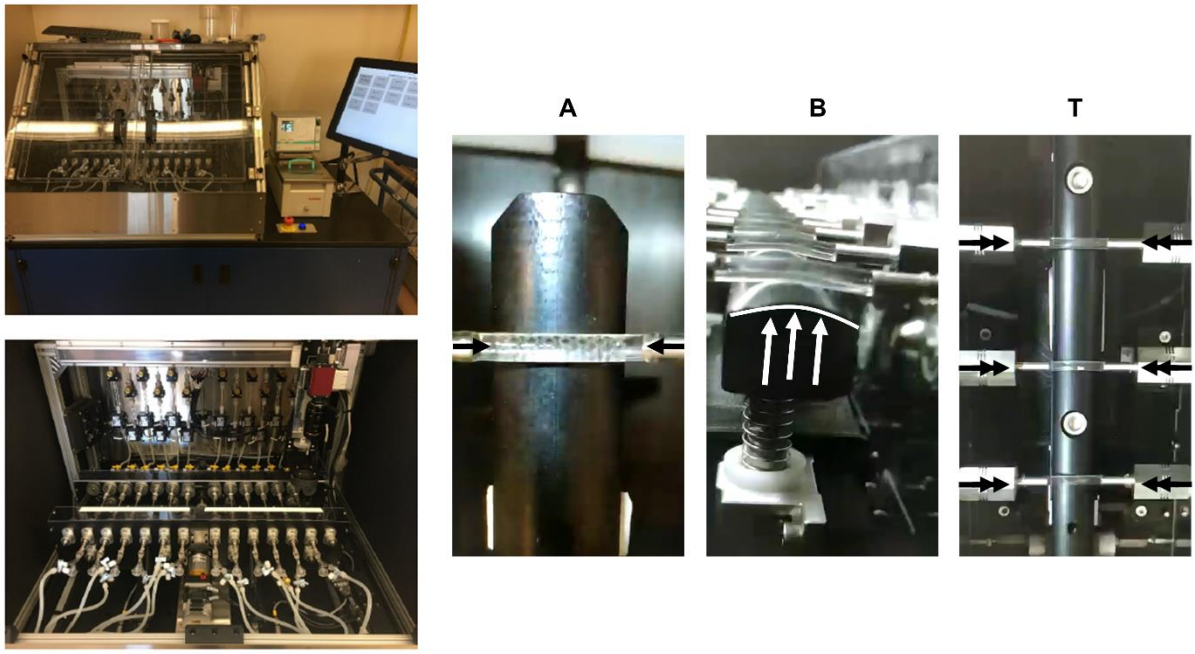

Figure 2 In-vitro benchtop setup for the multimodal loads application (left). On the right, an insight into the single loads: axial compression (A), bending (B), and torsion (T) applied to the silicone tubes with implanted scaffolds filled with phosphate-buffered saline.

A high-throughput multimodal fatigue test system was used to conduct all benchtop fatigue experiments. Scaffolds were removed from 4°C and kept at room temperature for at least one hour before the test. Then, they were inserted into and inflated inside compliant silicone vessels (Dynatek Labs, Galena, MO, diameter: 2.8 ± 0.2 mm) at a rate of one atm every two seconds to 12 atm, and the balloon maintained inflated for 30 seconds before deflation. This mimicked the clinical inflation protocol suggested by the manufacturer. The compliant silicone vessels were filled with phosphate-buffered saline (PBS) propelled at 40 – 50 ml/min within each vessel with a temperature stable at 37±1 ^{o}C. Flow rate was selected to maintain controlled pH environment and ensure physiologically relevant shear forces. Three modes of loads were applied to the mock

vessels to successfully reproduce fracture rate and location pattern, including 15° bending (B), 7° torsion (T) and 4% axial compression (A), at a frequency of 1 Hz for 14 days. These loads type are physiologically relevant, but their amplitudes were chosen to best-fit the animal study. Similarly, we examined devices at 14 days, instead of 30 as in the animal study, as preliminary evidence indicated that all scaffolds completely fractured within the 14 days and also to not extend mechanical strain so as to further distort devices.

Seven different combinations of loads were tested, including three combined loads (B+T+A, 7 scaffolds were tested for both non-slot and slot design), any two of the three loads (B+T, T+A, or B+A, 3 scaffolds were tested for non-slot design and 2 for slot design, for any load combination), and single-mode load (B, T, or A only, 3 scaffolds were tested for non-slot design and 2 for slot design, for any load). Tests were paused every 24 hours to scan for and record fractures. Only full separation of struts was considered as a fracture. Scaffolds were removed from the vessel after tests for a better inspection. Locations of fractures were sorted into three categories, namely, connected peak (Type I), unconnected peak (Type II), and connector (Type III) (Figure 3).

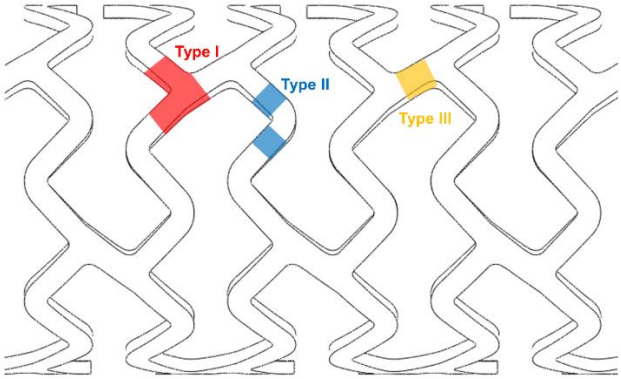

Figure 3 Fracture location categories: Type I – Connected peak (Red); Type II – Unconnected peak (Blue); Type III: Connector (Yellow).

4.3 FE Analysis on Stress Distribution under Multimodal Loads

Abaqus/Explicit 2018 (Dassault Systèmes, Providence, RI, USA) was used as a finite element software to determine high stressed locations in the scaffold under multimodal loads. Both designs were reconstructed in their expanded configuration through the commercial software Solidworks 2017-18 (Dassault Systèmes, Providence, RI, USA) starting from optical images (Figure 4, a). The discretization was created by Hypermesh (Altair Hyperworks): the non-slot design resulted in 242,785 linear hexahedral fully integrated elements (with incompatible mode formulation, C3D8I), with four elements designated across the strut thickness [19], and the slot design was prepared accordingly, with 233,208 elements. Material parameters for the numerical analysis were extracted from the previous true stress-true strain experimental curves obtained from submerged specimens [19]. Johnson-Cook plasticity model was employed to capture the non-linear material hardening behavior after yielding and the strong dependency on testing velocities. The temperature dependence of the model was deactivated as the tests were conducted well below the glass transition temperature and at a constant temperature setting. The yield stress $\bar{\sigma}$ is reported as:

$$\bar{\sigma} = [\, C_1 + C_2(\bar{\varepsilon}^{pl})^n][1 + C_3 \ln(\dot{\bar{\varepsilon}}^{pl}/\dot{\varepsilon}^0)]$$

where $\bar{\varepsilon}^{pl}$ is the equivalent plastic strain, C_1, C_2, C_3 n and $\dot{\varepsilon}^0$ are material parameters of the model and $\dot{\bar{\varepsilon}}^{pl}$ is the equivalent plastic strain rate (a brief recap of the chosen material parameters is given in Table 1). All the stress measurements are provided according to the von Mises stress.

Table 1 Material model parameters employed in this study, characterized in [18]

Elastic Modulus (MPa)	C_1 (MPa)	C_2 (MPa)	C_3 (MPa)	n	$\dot{\varepsilon}_0$ (1/s)
1400	59	205	0.11	1.4	0.0002

The simulation set-up strived to mimic a real clinical intervention scenario. The time-scaling factor has been set to one with a target time increment of 1×10^{-5}. Interaction between all the surfaces was defined as "general contact" with a friction coefficient of 0.2. The framework of the simulation and its steps could be described as follow:

1. Crimping: The unconstrained scaffold (density = 1.4 g/cm^3) was radially compressed by 16 external discrete rigid planes (R3D4, 272 elements). 1 mm radial displacement was applied. The step time was 60 s in accordance with the previous analysis (Figure 4, b).

2. Release: The planes were removed to let the scaffold recoil freely. The step time was 10 s.

3. Intraluminal positioning and pre-stretch: The crimped scaffold was positioned inside a mock vessel (density = 1.16 g/cm^3, E = 7 MPa, Poisson's ratio = 0.45, internal lumen diameter = 3.0 mm, thickness = 0.5 mm, modeled as a deformable shell, S4 8,442 elements). The mock vessel was pre-stretched by applying an axial displacement of 0.5 mm to both its ends through Multi Points Constraints (MPCs). The step time was 1 s.

4. Inflation: A folded balloon (density = 1.16 g/cm^3, E= 375 MPa, Poisson's ratio = 0.45, initial diameter = 1.0mm, 14,280 elements, M3D4, thickness = 0.03mm) was inflated

up to 12 atm internal pressure to radially expand the scaffold. The step time was 24 s, mimicking the in-vitro procedure (Figure 4, c).

5. Relaxation: The balloon was maintained at the expanded state with the step time of 30 secs to allow stress relaxation in the scaffold.

6. Recoil: The balloon was deflated up to 0 atm pressure to allow free recoil. The step time was 1 s (Figure 4, d).

7. Loading: Multimodal loads were applied to the tube mimicking the experimental setups. The axial compression (A) and torsion (T) were applied at the MPCs of the mock vessel as in the in-vitro tests. The bending action (B) was simulated through the lateral impact of a curved rigid surface (curvature radius = 15°, length = 17.78 mm, SFM3D4R, 38,100 elements) on one side of the tube. The vertical movement of 1 mm led the curved surface to deform the tube in a three-point-bending way (Figure 4, e). The step time was 1 s.

Then, the last step was modified to apply the isolated loads (A, T, or B only) and successively the same in combination (B+A, A+T, and B+T) to better understand the role of the single contribution to the fracture locations.

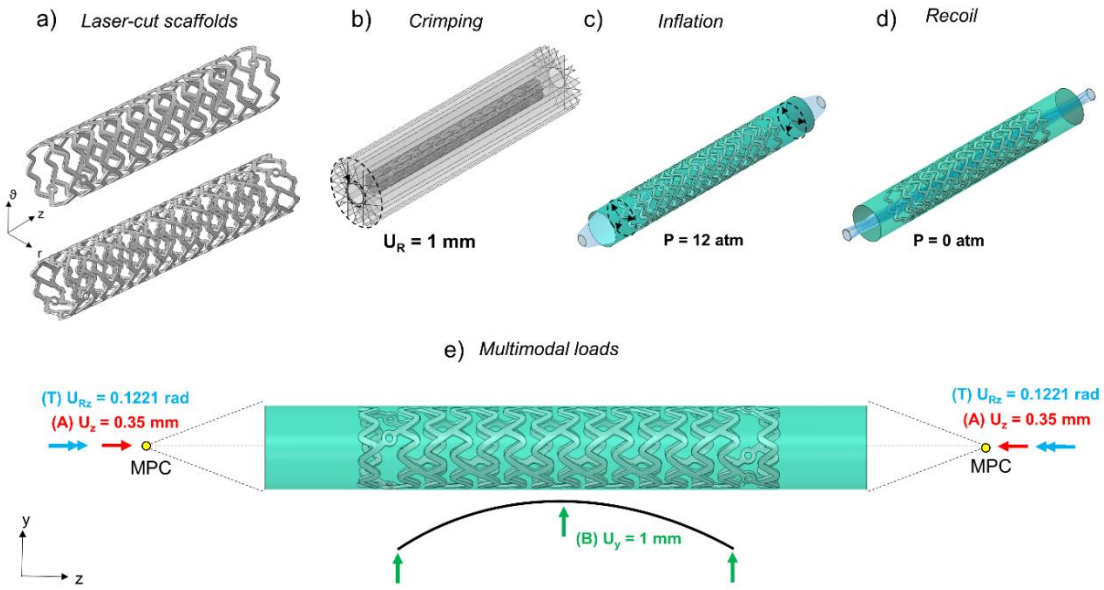

232

233 **Figure 4** Simulation steps involving the a) laser-cut scaffold geometry designed in
234 Solidworks; b) a crimping phase reduces the outer diameter of 1 mm; c) a folded balloon
235 is expanded by a 12 atm internal pressure to expand the scaffold inside the silicone vessel;
236 d) the balloon is deflated and the scaffold is located inside the mock vessel; e) multimodal
237 load combination of axial compression, bending, and torsion.
238
239

5. Results

5.1 Pre-clinical Studies on Scaffold Fractures

Two fractures, both type I, were found amongst the 8 slot designs tested (0.25 fractures per scaffold) while 54 fractures were found in the 8 non-slot designs (6.75 fractures per scaffold) (Figure 5, Table 2). Of the 54 fractures in non-slot designs, 32 were type I and 22 type II.

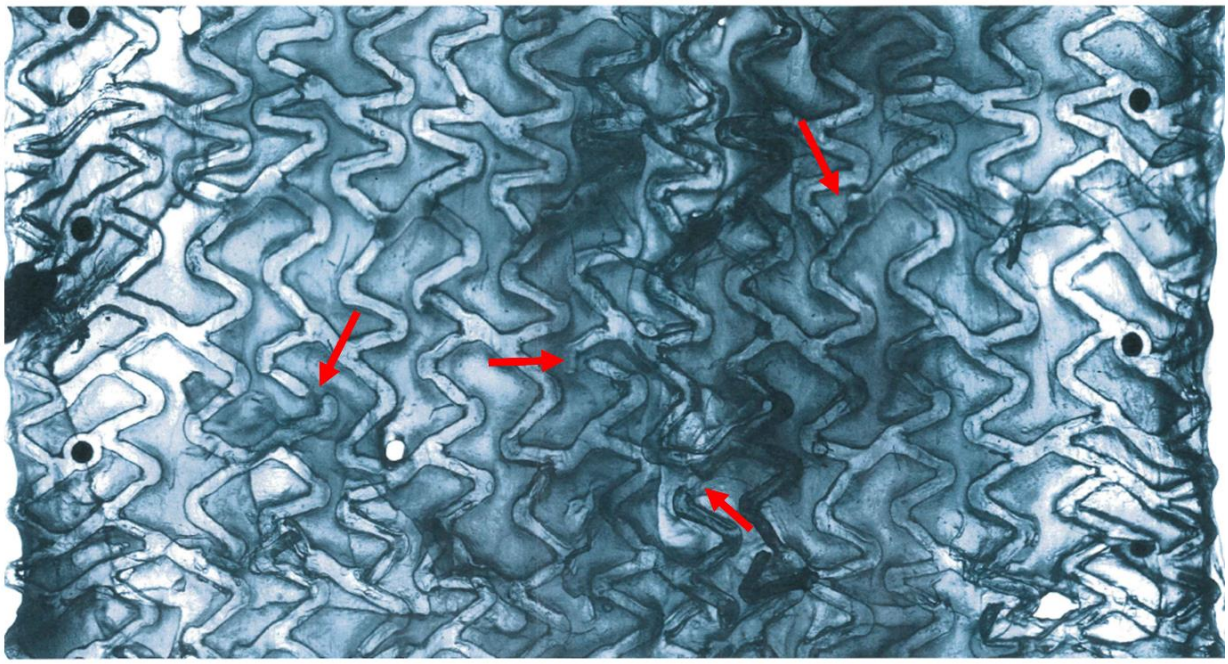

Figure 5 Visicon image of a fractured scaffold, 30-day post-implantation, non-slot design. Red arrows highlight some fracture locations.

5.2 Benchtop Durability Test with Multimodal Loading Environment

Only one fracture (Type I, load condition = B+A) was found among the tested slot-design scaffolds. Among all 25 non-slot designs, 43 fractures were found. Only one fracture (Type I, load condition = bending only) was found among 9 scaffolds tested in single-mode load condition. A total of 25, 8, 6, and 3 fractures were found in each test

configuration when two or more load types were applied (Table 2). Fracture locations changed significantly with load modes. When all three loads were applied (B+T+A), type I was the dominant fracture type followed by type II and III. When torsion was removed (B+A), fracture rate decreased but the location pattern maintained at a similar trend. However, when bending or axial compression were removed, the fracture location pattern changed completely: type II became dominant, while type I was largely reduced (B+T) or even disappeared (T+A).

Table 2 Fractures found in non-slot design when two or more loads were applied (n = number of tested scaffolds).

Three loads combined						Two loads combined					
	n	I	II	III	All		n	I	II	III	All
In-vivo	8	32 (60%)	22	0	54	B+A	3	5 (63%)	3	0	8
B+T+A	7	17 (68%)	8	0	25	T+A	3	0 (0%)	6	0	6
						B+T	3	1 (33%)	2	0	3

5.3 FE Analysis of Stress Distribution with Multimodal Loading

The element volume fraction (#elements/total #elements) for those experiencing high stresses (> σ_{yield} ~ 60 MPa) was almost twice as much in the non-slot designs as in the slot designs after crimping, inflation, and recoil (5.1% vs 2.9%). The element volume fraction experiencing critical stresses (>150 MPa) was compatible in both geometries (around 0.1%) (Figure 6). Based on a previous study [19], 60 and 150 MPa was associated with the yield stress and ultimate tensile strength of the material.

After crimping and inflation and with all the loads applied, the element volume fraction for those experiencing high stresses (> σ_{yield}) became 8.7% for the non-slot design and 6.2% for the slot one. The element volume fraction for elements undergoing critical

stresses (>150 MPa) was higher in the non-slot design (1.4% vs 0.2%) (Figure 7).

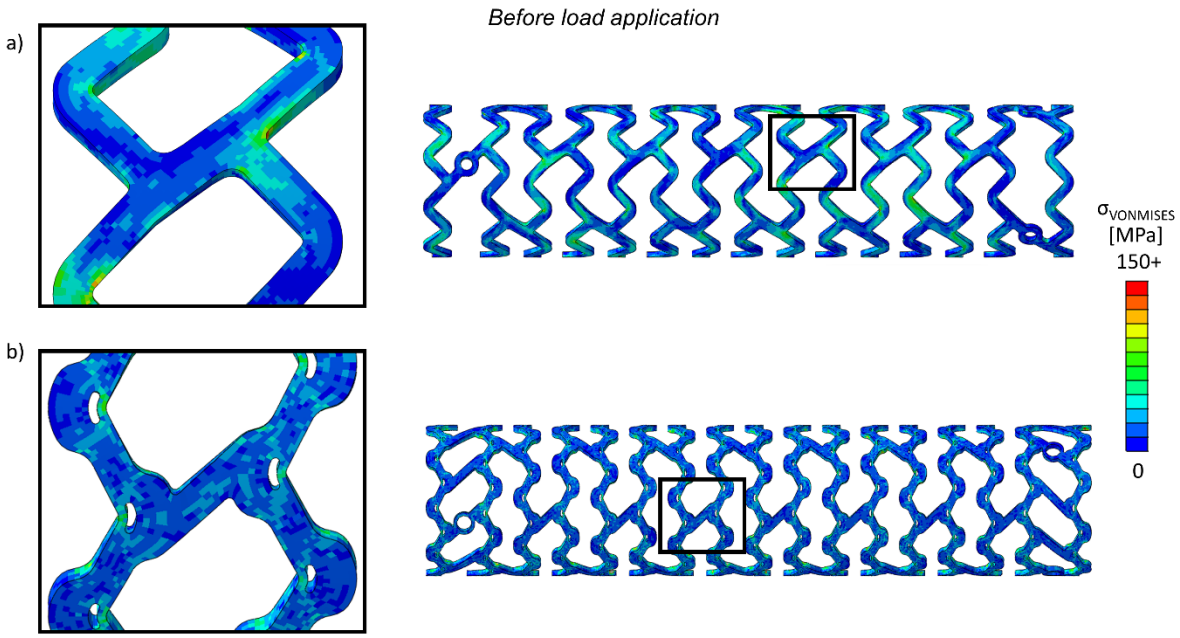

Figure 6 Stress distribution in a) non-slot and b) slot designs before load application. Stresses concentrated at peak features with more elements experiencing high stresses (> σ_{yield}) in non-slot designs than in slot designs.

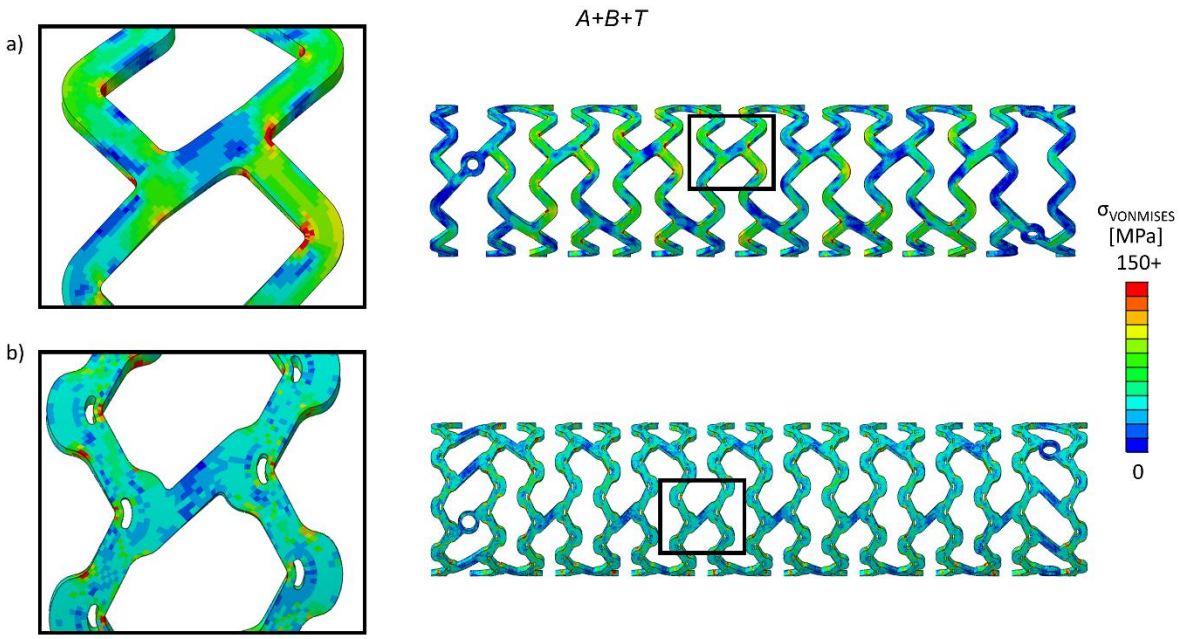

Figure 7 Stress distribution in a) non-slot and b) slot designs during the loads application (B+T+A). Stresses, for non-slot designs, concentrated at peak features with more elements experiencing high stresses (> 150 MPa) than for slot designs.

Stress concentrators changed when different isolated loads were applied after crimping, inflation, and recoil (Figure 8, top row). With bending applied, stress concentrated at both inner and outer edges of connected peaks (explaining Type I fracture), reaching quite critical values for damaging the structure (>100 MPa). With axial compression and torsion applied, no evident stress concentration was detected and a beneficial effect was observed (lowered stress values) in accordance with the benchtop tests which showed no fracture. In combined two-load scenarios (Figure 8, bottom row), when torsion and axial compression were applied, stress concentrated entirely at unconnected peaks (explaining Type II fracture). When bending and torsion were applied, stress concentrated at both connected (explaining Type I fracture) and unconnected peaks. When bending and axial compression were applied, higher stresses (>100 MPa) concentrated at connected peaks and unconnected peaks: the axial compression seems to play a beneficial role compared to the case in which the sole bending is applied. Stress concentrators predicted herein with simulations are consistent with fracture locations found in benchtop experiments at each loading scenario.

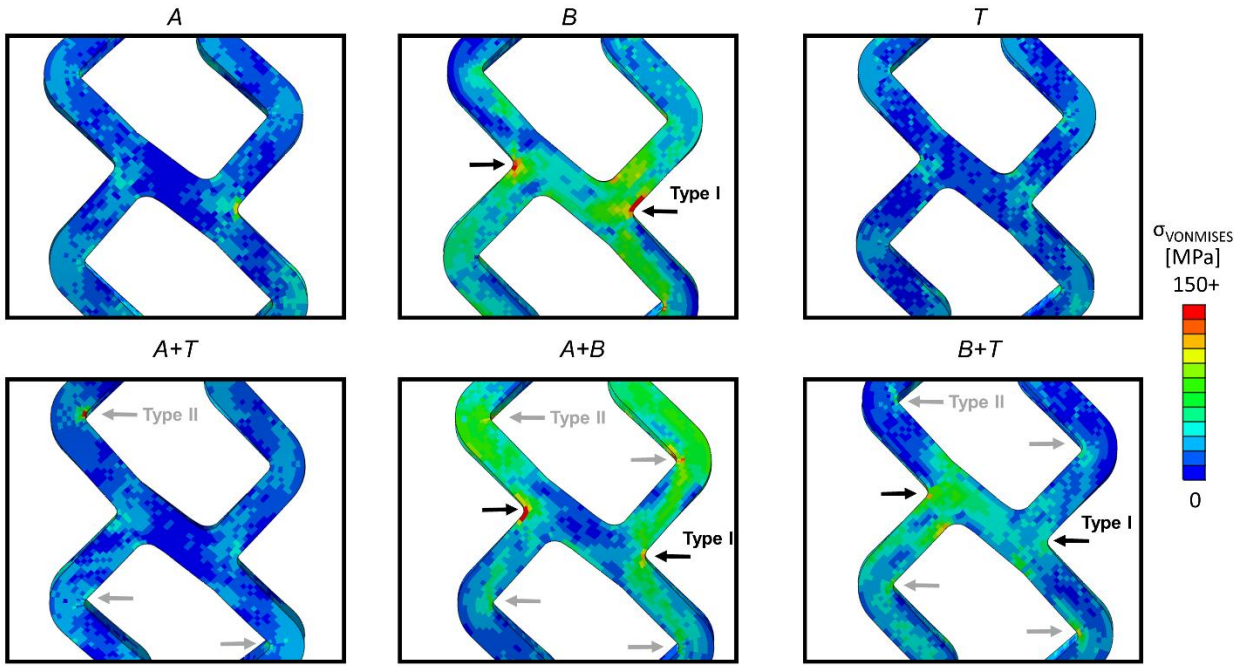

Figure 8 Stress concentrators at isolated load conditions (B+T+A) and combined load scenarios (A+T, A+B, and B+T), showing a good match with the experimented in-vitro and in-vivo fracture locations.

6. Discussion

Bioresorbable scaffolds are expected to withstand tens of millions of cycles of multimodal loads after implantation without major structural failures until resorption starts. Such durability tests traditionally employ single-mode cyclic loads [3,4,11] raising the question as to whether potential failure modes may be overlooked when benchtop tests fail to capture the physiological environment. Single-mode cyclic loads oversimplify vessel anatomy and dynamics, and lesion features, and thus overestimate devices' resistance to environmental loads. This could result in a reduced failure rate reported by benchtop experiments and disparity with preclinical tests mandating further animal studies and potentially misleading design of clinical studies. Such risk may be even more profound when it comes to characterizing BRS behavior as the degradation of these devices also depends on external loading conditions [11]. Poorly understood degradation profiles may lead to unexpected early structural failures *in vivo* when complex environmental loads present. In addition, animal tests are often not adequate replicate of clinical condition, as healthy animal arteries have limited capabilities to mimic the complex in-vivo environment in real-world patients.

The combination of the high-throughput multimodal benchtop system and the properly designed in-silico model offers a powerful tool to investigate implanted device behaviors in a more realistic loading environment. The multimodal benchtop system applies isolated or combined deformation modes evident in-vivo in a flow- and temperature-controlled environment and reveals potential failure modes of tested substrates. The *in silico* model, if accurately designed, links the applied loading environment with the failure modes in a quantitative and analytical way. Such platforms are capable to predict not only the

incidence and frequency of modes of failure, but also selectively localize them.

Alternative designs, as showed by slot scaffolds, could eliminate or alleviate expected failure modes. However, updated benchtop set-ups and physiology-informed loading package for computations are mandated to reach such a design and test it to minimize the adverse clinical outcomes. The deformation modes can as well be customized to adapt different load patterns in-vivo. The use of mock arteries to enclose scaffolds allows loads to be applied uniformly along the length of the scaffold and avoids stress concentration caused by fixtures. They can accommodate different sizes of devices and even incorporate different lesion configurations and tissue states in the future to better capture the in-vivo pathological environment. The entire testing procedure should though mimic the implantation process during clinical practices to avoid undesirable mechanical input during specimen preparation.

It is worth adding that the load history (crimping, inflation, and recoil in the vessel) cannot be neglected since the residual state of stress and strain was severely altered by the procedure itself (Figure 6) [18,19]. Cyclic loads added contributions over an already deformed/loaded configuration. Some combinations resulted beneficial while others were detrimental and probably may accelerate the crack propagation (Figure 8).

Slot design effectively reduced the stress level across the scaffold: less number of elements was experiencing critical stresses (>150 MPa) than in the former non-slot design (Figure 7). In addition, high stressed elements were mostly concentrated around the slot features, especially at the connection piece linking the inner edges of the peak feature (Figure 7b). This design is intended to break and release high stresses to prevent

the propogation of cracks through the entire strut. Significant lower number of fractures were seen in slot design scaffolds in both animal and benchtop studies, indicating the fact that reducing stress concentration via certain design features can effectively prevent early structural failures.

With loads applied individually, almost no fracture was identified in both designs, which confirmed that traditional benchtop testing strategies utilizing single-mode loads are not sufficient. Once multimodal loads were applied, fractures started to emerge (Table 2). In this way, the evaluation of scaffold durability becomes more robust, and hidden design flaws can be identified before animal studies. In addition, variations in fracture locations were seen when different combinations of loads were applied. The location pattern in benchtop tests and animal studies matched when at least bending and axial compression are applied. This is due to the changes in stress concentrators with different loading types (Figure 8) and indicates the possibility of predicting locations with a high risk of fracture based on specific vessel geometries and dynamics employing in-silico tools.

There are some limitations that need to be overcome in the near future toward the definition of an optimally reliable predictive tool. In particular, the FE model is not accounting any degradation phenomena, since they were assumed negligible in a short-term follow-up considered herein. Moreover, fracture propagation was not simulated. More accurate material definitions, including degradation and fracture parameters, should be selected and properly calibrated on an experimental campaign on proper specimens, should we consider monitoring the durability in long term. In addition, long-term in-vivo studies can be conducted to evaluate each device's degradation profile and how the

external loading conditions can alter the degradation rate. When combined with intrinsic heterogeneities in material properties, external loads may lead to severe non-uniform degradation at certain design features, causing localized flow disruption and clinical events [18].

Performing the present work, we reemphasized that microstructural damages and micro-cracks should be considered as potential initiators of scaffold fracture and failures. These damages are caused by stress concentration and can be very well prevented through design optimization. However, this requires redefining the evaluation criteria for scaffold fracture. In addition, load types contribute to crack propagation and fracture locations. Ignoring the necessity of incorporating a multi-modal loading environment into benchtop fatigue tests will lead to overlook potential design defects. With a thorough understanding of vessel dynamics and lesion morphology, combined with the robust testing method we presented here, we may be able to design scaffolds optimized to a patient-specific working environment.

7. Conflicts of Interest

The authors declare that there are no conflict of interests regarding the publication of this article.

8. Ackowledgements

The authors gratefully thank Boston Scientific Corporation (Marlborough, MA) for partial grant support and generous supply of test specimens and scaffolds, and the supports of animal studies. Elazer R Edelman, Pei-Jiang Wang, and Farhad Rikhtegar Nezami were supported in part by National Institutes of Health (R01 49039). Francesca Berti and Francesco Migliavacca were partially supported by the Fondazione Fratelli Agostino and Enrico Rocca through a “Progetto Rocca” doctoral fellowship. Francesca Berti, Luca Antonini, Lorenza Petrini, and Francesco Migliavacca are partially supported by the European Project INSILC.

9. References

1. Ali, Z. A., R. Gao, T. Kimura, Y. Onuma, D. J. Kereiakes, S. G. Ellis, B. Chevalier, M. T. Vu, Z. Zhang, C. A. Simonton, P. W. Serruys, and G. W. Stone. Three-Year Outcomes with the Absorb Bioresorbable Scaffold. *Circulation* 137:464–479, 2018.
2. Ang, H. Y., Y. Y. Huang, S. T. Lim, P. Wong, M. Joner, and N. Foin. Mechanical behavior of polymer-based vs. metallic-based bioresorbable stents. *J. Thorac. Dis.* 9:S923–S934, 2017.
3. ASTM International. ASTM F2606-08: Standard Guide for Three-Point Bending of Balloon Expandable Vascular Stents and Stent Systems. 2008.
4. ASTM International. Standard Test Methods for in vitro Pulsatile Durability Testing of Vascular Stents. 2013.
5. Bergström, J. S., and D. Hayman. An Overview of Mechanical Properties and Material Modeling of Polylactide (PLA) for Medical Applications. *Ann. Biomed. Eng.* 44:330–340, 2016.
6. Byrne, R. A., G. G. Stefanini, D. Capodanno, Y. Onuma, A. Baumbach, J. Escaned, M. Haude, S. James, M. Joner, P. Jüni, A. Kastrati, S. Oktay, W. Wijns, P. W. Serruys, and S. Windecker. Report of an ESC-EAPCI Task Force on the evaluation and use of bioresorbable scaffolds for percutaneous coronary intervention: Executive summary. *EuroIntervention* 13:1574–1586, 2018.
7. Cheng, Y., P. Gasior, K. Ramzipoor, C. Lee, J. C. McGregor, G. B. Conditt, T. McAndrew, G. L. Kaluza, and J. F. Granada. In vitro mechanical behavior and in vivo healing response of a novel thin-strut ultrahigh molecular weight poly-L-lactic

acid sirolimus-eluting bioresorbable coronary scaffold in normal swine. *Int. J. Cardiol.* 286:21–28, 2019.

8. Choi, G., C. P. Cheng, N. M. Wilson, and C. A. Taylor. Methods for quantifying three-dimensional deformation of arteries due to pulsatile and nonpulsatile forces: implications for the design of stents and stent grafts. *Ann. Biomed. Eng.* 37:14–33, 2009.

9. Choi, G., G. Xiong, C. P. Cheng, and C. A. Taylor. Methods for characterizing human coronary artery deformation from cardiac-gated computed tomography data. *IEEE Trans. Biomed. Eng.* 61:2582–92, 2014.

10. Ding, Z., H. Zhu, and M. H. Friedman. Coronary Artery Dynamics In Vivo. *Ann. Biomed. Eng.* 30:419–429, 2002.

11. Dreher, M. L., S. Nagaraja, and B. Batchelor. Effects of fatigue on the chemical and mechanical degradation of model stent sub-units. *J. Mech. Behav. Biomed. Mater.* 59:139–45, 2016.

12. Kolandaivelu, K., and F. Rikhtegar. The Systems Biocompatibility of Coronary Stenting. *Interv. Cardiol. Clin.* 5(3):295-306, 2016.

13. Liao, R., N. E. Green, S.-Y. James Chen, J. C. Messenger, A. R. Hansgen, B. M. Groves, and J. D. Carroll. Three-Dimensional Analysis of in vivo Coronary Stent – Coronary Artery Interactions. *Int. J. Cardiovasc. Imaging* 20:305–313, 2004.

14. Qiu, T., R. He, C. Abunassar, S. Hossainy, and L. G. Zhao. Effect of two-year degradation on mechanical interaction between a bioresorbable scaffold and blood vessel. *J. Mech. Behav. Biomed. Mater.* 78:254–265, 2018.

15. Schmidt, W., P. Behrens, C. Brandt-Wunderlich, S. Siewert, N. Grabow, and K. P.

Schmitz. In vitro performance investigation of bioresorbable scaffolds – Standard tests for vascular stents and beyond. *Cardiovasc. Revasc. Med.* 17:375–383, 2016.

16. Serruys, P. W., B. Chevalier, Y. Sotomi, A. Cequier, D. Carrié, J. J. Piek, A. J. Van Boven, M. Dominici, D. Dudek, D. McClean, S. en Helqvist, M. Haude, S. Reith, M. de Sousa Almeida, G. Campo, A. Iñiguez, M. Sabaté, S. Windecker, and Y. Onuma. Comparison of an everolimus-eluting bioresorbable scaff old with an everolimus-eluting metallic stent for the treatment of coronary artery stenosis (ABSORB II): a 3 year, randomised, controlled, single-blind, multicentre clinical trial. *Lancet* 388:2479–2491, 2016.

17. Sotomi, Y., P. Suwannasom, P. Serruys, and Y. Onuma. Possible mechanical causes of scaffold thrombosis: insights from case reports with intracoronary imaging. *EuroIntervention* 12:1747–1756, 2017.

18. Wang, P. J., N. Ferralis, C. Conway, J. C. Grossman, and E. R. Edelman. Strain-induced accelerated asymmetric spatial degradation of polymeric vascular scaffolds. *Proc. Natl. Acad. Sci. U. S. A.* , 2018.doi:10.1073/pnas.1716420115

19. Wang, P. J., F. R. Nezami, M. B. Gorji, F. Berti, L. Petrini, T. Wierzbicki, F. Migliavacca, and E. R. Edelman. Effect of working environment and procedural strategies on mechanical performance of bioresorbable vascular scaffolds. *Acta Biomater.* 82:34–43, 2018.